Impact of the Fused Deposition (FDM) Printing Process on Polylactic Acid (PLA) Chemistry and Structure

Authors

Michael A. Cuiffo[1], Jeffrey Snyder[2], Alicia M. Elliott[1], Nicholas Romero[3], Sandhiya Kannan[1] and Gary P. Halada[1,*]

[1] Department of Materials Science and Chemical Engineering, Stony Brook University, Stony Brook, NY 11794-2275

[2] Department of Physics, SUNY New Paltz, New Paltz, NY, 12561

[3] Department of Materials Science and Engineering, Binghamton University, Binghamton, NY, 13901.

[*]Corresponding author contact information: Engineering Bldg. Rm 308, Department of Materials Science and Engineering and Chemical Engineering, Stony Brook University, Stony Brook, NY 11794-2275; Tel: 631-632-8526; Fax: 631-632-8052; e-mail: gary.halada@stonybrook.edu.

Abstract

Polylactic Acid (PLA) is an organic polymer commonly used in fused deposition (FDM) printing and biomedical scaffolding that is biocompatible and immunologically inert. However, variations in source material quality and chemistry make it necessary to characterize the filament and determine potential changes in chemistry occurring as a result of the FDM process. We used several spectroscopic techniques, including laser confocal microscopy, Fourier-Transform

Infrared (FTIR) spectroscopy and photoacousitc FTIR spectroscopy, Raman spectroscopy, and X-ray photoelectron Spectroscopy (XPS) in order to characterize both the bulk and surface chemistry of the source material and printed samples. Scanning Electron Microscopy (SEM) and Differential Scanning Calorimetry (DSC) were used to characterize morphology, crystallinity, and the glass transition temperature following printing. Analysis revealed calcium carbonate-based additives which were reacted with organic ligands and potentially trace metal impurities, both before and following printing. These additives became concentrated in voids in the printed structure. This finding is important for biomedical applications as carbonate will impact subsequent cell growth on printed tissue scaffolds. Results of chemical analysis also provided evidence of the hygroscopic nature of the source material and oxidation of the printed surface, and SEM imaging revealed micro and sub-micron scale roughness that will also impact potential applications.

Keywords

PLA; fused deposition modeling (FDM); surface characterization; vibrational spectroscopy; laser confocal microscopy; X-ray photoelectron spectroscopy

Introduction

3D printing is an emerging technology that can be used to construct complex structures inexpensively for modeling, prototyping, or production through deposition or solidification. Fused deposition modeling (FDM) is a standard method for 3D printing using thermoplastic feedstock, in which heated extruders deposit material in patterns determined by translated computer-assisted design (CAD) files, and build up structures layer by layer, (1).

Polylactic acid (PLA) is a racemic mixture of D and L lactide (2, 3), an aliphatic polyester thermoplastic derived from starches of corn, and sugarcane. PLA is immunologically inert (4) as it gradually degrades into innocuous lactic acid over time (six months to 2 years) (5) making it attractive for use in the field of medicine, such as for medical implants (screws, pin, rods, and meshes) (6). Also, PLA has a low glass transition temperature (T_g = 60 – 65 °C) and melting temperature (T_m = 173 – 178 °C), making it very useful for 3D printing since it does not require a heated surface for the objects being printed.

Materials and Methods

Fused Deposition (FDM) Printing

Makerbot Replicator and Replicator 2X FDM-type 3D printers in conjunction with Makerware software version 2.4.1.62 were used to build 1.0 cm^2 x 0.2 cm thick PLA samples from natural 1.75 mm PLA filament (Nature Works). Printing parameters were set to standard (0.2 mm) or high (0.1 mm) resolution (100-200 micron) with an extruder temperature of 229°C and an extrusion speed of 90 mm/s with 150 mm/s traveling speed. The printer extruder head deposits the melted PLA layer by layer with the aid of rafts or support structures to create the intended structure. All materials were handled with gloved hands and following standard surface analysis laboratory practices to minimize any possible contamination.

Optical Microscopy

All optical images were collected with an Meiji optical microscope with a Nikon DXM 1200 digital camera and a 0.6 X HRD 060-CMT by Diagnostic Instruments using ACT 1 version 2.20 – software. Images were also collected from test samples before and after Raman

microspectroscopy to compare the overall appearance of areas analyzed to their respective chemical spectra. This also aided in ensuring no damage had been induced by the Raman laser.

Scanning Electron Microscopy (SEM)

The SEM system used was a LEO 1550 microscope equipped with a Robinson backscatter Gemini detector with Energy dispersive x-ray analysis (EDAX), as well as AC, EBSP, SE, and InLens detectors. SEM was used primarily for determining surface morphology.

Confocal Microscopy

Confocal microscopy data was collected with an upright Leica DM 6000 microscope, with adaptive focus, motorized XY-Stage (15 nm step size) and Super Z Galvo (1500µm/ 3 nm step size). The system is equipped with an 8 khZ tandem scanner and both white light (470-670 nm) and UV (405 nm) lasers, capable of providing a 400-800 nm detection range for fluorescence imaging. The sample was mounted on a non-fluorescing slide, and the filament and finished print were imaged using a 10x objective and UV laser excitation (405 nm).

Raman Spectroscopy

Raman analysis was conducted using an Almega Dispersive Raman Microscope (Thermo Nicolet) with a 785 nm laser source. Alignment of the laser and all the optical components was conducted prior to analysis. The detector was cooled to –50°F throughout the experiment. The samples were analyzed with 64 cumulative scans with optimized laser power, aperture size, and duration (1- 6 seconds) per exposure in order to achieve the best signal to noise ratio, and/or spot size. All analyzed locations of the respective samples analyzed by Raman spectroscopy had their

color, texture, laser power, and aperture size recorded and several were photographed using the optical microscope and camera. Throughout the Raman analysis the laser power was kept below 50% in order to insure no thermal damage was induced as reported by de Faria (7), and Hanesch (8). Our previous work has shown that lowering Raman laser intensity can preserve even samples known to be thermally unstable (9). Samples were placed on a quartz microscope slide (Ted Pella) which is Raman inactive and therefore will not produce any spurious peaks in the analyzed samples.

Fourier Transform Infrared (FTIR) Spectroscopy

FTIR was conducted with a Nicolet 560 IR spectrometer or an iS50 FTIR spectrometer, both using a liquid nitrogen cooled MCT-A detector or a DGTS detector (at room temperature) with data resolution summed over 256 scans for a better signal to noise ratio. Sampling areas were continuously purged with dry air throughout the experiments in order to prevent the additional absorption of water vapor in the samples being analyzed.

Photoacoustic Fourier Transform Infrared (FTIR) Spectroscopy

Photoacoustic FTIR analysis was done using an MTEC PAC 300 detector on the Nicolet 560 IR, and Nicolet IS50 FTIR spectrometers. The sample chamber was purged using ultra high grade purity helium gas. All scans were taken summing between 8 – 32 exposures for a better signal to noise ratio.

X-ray Photoelectron Spectroscopy (XPS)

XPS was conducted using a custom-designed system with an X-ray source from PHI Electronics (10-12 KV at 10 m amps at 65-75 Watts) with a spectrometer utilizing a V.G. Scientific (Fisons) CLAM 100 hemispherical analyzer with a VGX900I controller data collection system. The X-

ray source was Al $K\alpha_{1,2}$ (1486.6 eV) with a pass energy of 20 or 50 eV, and 100 eV for the wide scan only and a work function of 4.55 eV. All XPS analysis was conducted at an ultrahigh vacuum of 1.0 x 10^{-9} to 1.0 x 10^{-8} torr. All XPS Spectra were taken at 90° take off angle with respect to the sample surface and all spectra were corrected for charging by using the C 1s line of adventitious carbon at 284.6 eV as a reference. All curve fitting followed the methods outlined by Savitsky and Golay (10), and Sherwood (11) as well as procedures developed over the years by G. P. Halada and C.R. Clayton (12-14) using CASA Software version 1.001. XPS was performed on select samples to determine the surface (depth analysis 5-10 nm) chemical changes taking place on the spool material and the resulting printed 3d structures.

Differential Scanning Calorimetry (DSC)

Differential Scanning Calorimetry (DSC) was conducted using a TA Instruments Q2000 (15), under a 20 mm/min nitrogen atmosphere. All samples were weighed prior to the experiment and all were to be approximately 10 mg. The heat was increased at a rate of 10°C per minute and reached a maximum temperature of 210ºC and then reversed in a cooling phase of 5ºC per minute to reach a final temperature of 25ºC. This data was used to generate a graph of heat flux versus temperature.

Results and Discussion

Optical Microscopy

Optical microscope imaging of the test samples was used to determine surface morphology, location of pores or any other potential defects that can occur in the printed samples at different printing resolutions. Three printing resolutions were used: low (0.3mm), standard (0.2 mm) and high (0.1 mm).

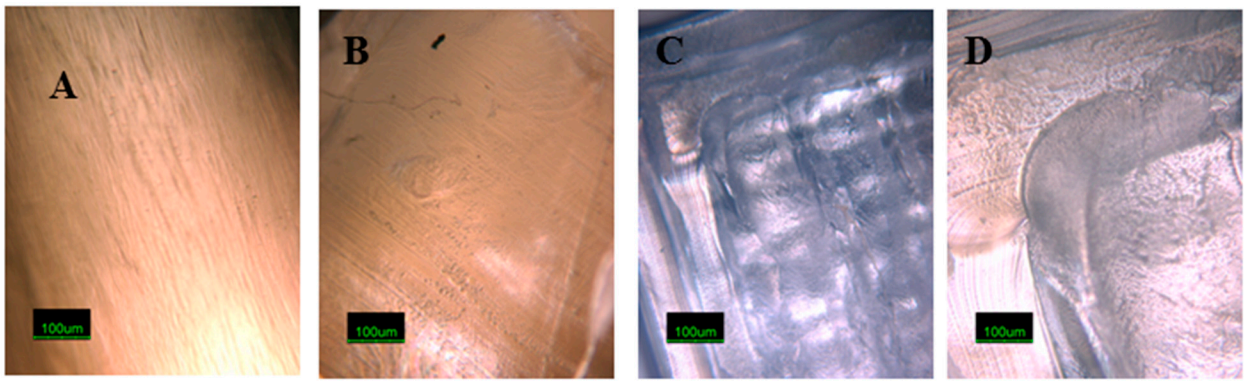

Figure 1: Optical microscope images: A) imaged of the PLA spool material. B) Cross-section of PLA Spool Material. C & D) are images at different magnifactions of the corner surface of a printed PLA test sample.

Figure 1 A and B are microscope images of the PLA spool material, lengthwise section and cross-section respectively. It can be observed that the spool material has noticeable features

Figure 1: Optical imaged of source and printed PLA.

process. Figure 1 C and D are microscope images of a corner of a 3 D printed test sample at different magnifications, highlighting the porous nature and roughness of the material.

Scanning Electron Microscopy (SEM) Results

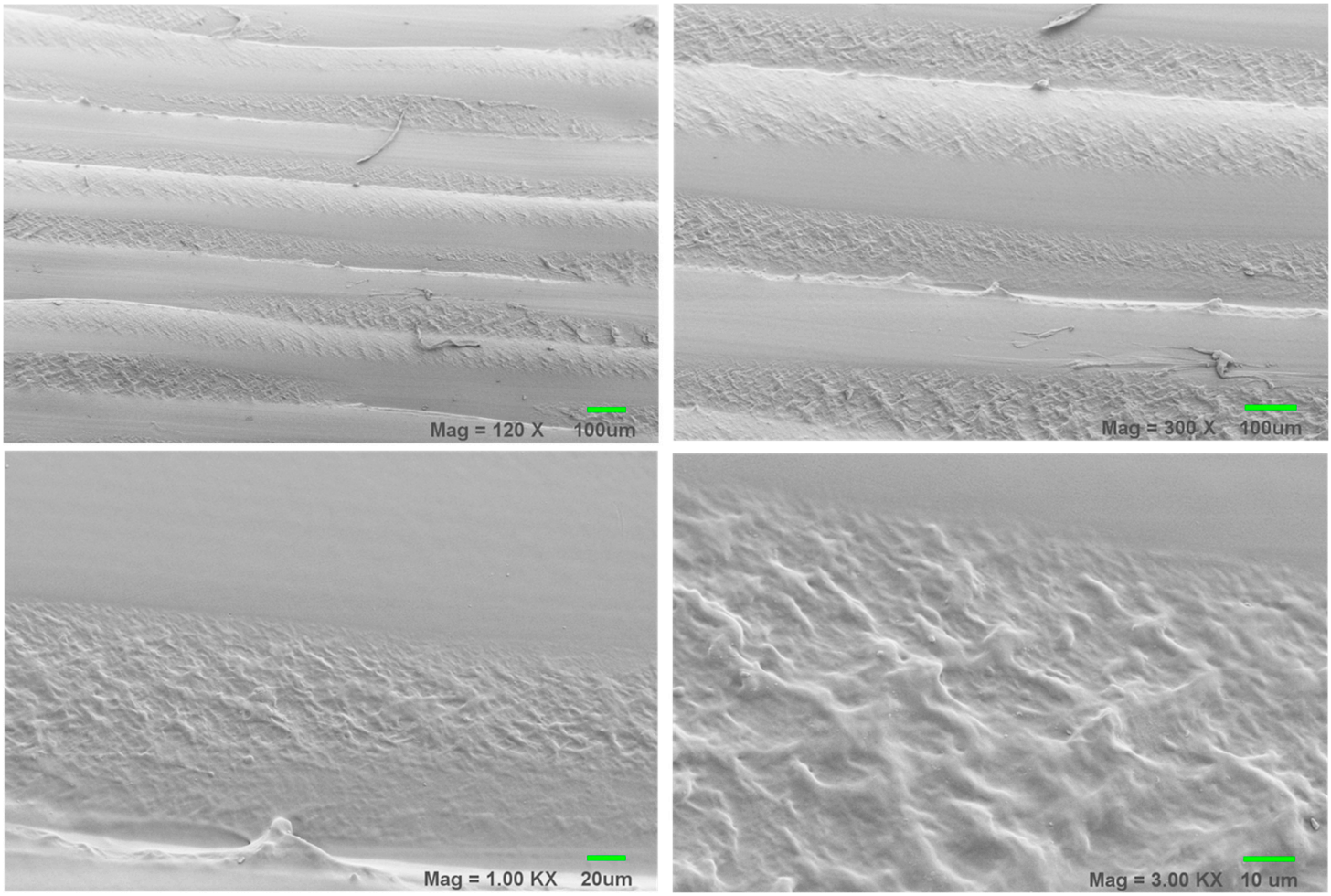

Figure 2: Scanning electron microscopy images of printed PLA showing micro and sub-micron scale roughness.

The SEM images in figure 2 show the morphology of the PLA 3d printed test samples with increasing magnification. At 120 X magnification it is clear that the extruded PLA at standard (0.2 mm) resolution fused well; however, it can be noted that integrated filaments had a micron and sub-micron scale roughness (which as noted later may be beneficial for cell adhesion and growth when used in scaffolding applications (16,17)). The ridged structure likely results from the movement of the print head during extrusion and cooling, and may be affected by the retention of heat in the sample.

Preprints (www.preprints.org) | NOT PEER-REVIEWED | Posted: 3 April 2017 doi:10.20944/preprints201704.0010.v1

Peer-reviewed version available at Appl. Sci. 2017, 7, , 579; doi:10.3390/app7060579

Laser Confocal Microscopy:

Laser confocal microscopy was used in order to identify any possible fluorescing species present in the filament or the printed sample. In general, microchemical analysis, combined with large area surface-sensitive spectroscopies and imaging, has proved to be essential for understanding the mechanisms controlling processing-performance relationships (18). Figure 3 shows a side view of the source filament. Clearly, there are fluorescing species visible (seen as bright green patches) on the surface of the filament, fairly evenly distributed.

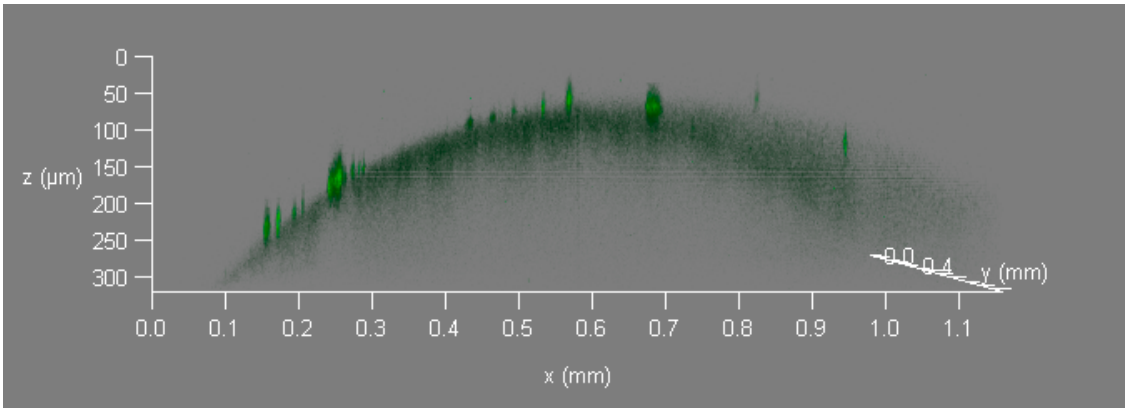

Figure 3: Laser confocal image of PLA source filament, collected from a side view with a 10x objective.

Figure 4 shows a top view of a printed PLA sample. Again, bright fluorescing areas are evident, mostly about 5 -30 microns in size (the one larger streak being about 15x115 microns). However, most of the fluorescent materials are concentrated in the dark voids in the 3D print. Views from a number of regions on the sample surface showed the same thing. Hence, whatever

process may have led to the formation of voids in the surface most likely also either preserved or

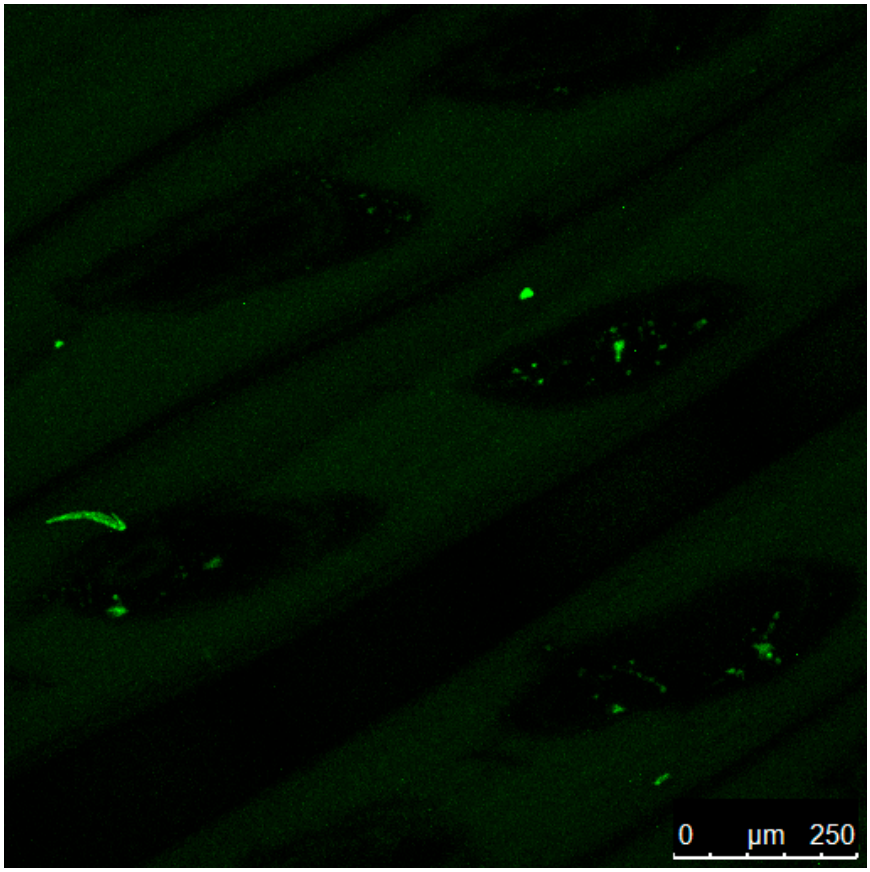

preferentially concentrated the fluorescent material.

Figure 4: Laser confocal microscope image of top surface of a printed PLA sample

In determining what species are fluorescing under irradiation by the 405nm wavelength laser, we use a combination of vibrational and electron spectroscopies (as detailed below) and x-ray fluorescence (XRF) using a Niton XL3t Thermoscientific system. XRF from the source filament and the printed samples show a number of similarities, as indicated in Table 1.

Preprints (www.preprints.org) | NOT PEER-REVIEWED | Posted: 3 April 2017 doi:10.20944/preprints201704.0010.v1

Peer-reviewed version available at Appl. Sci. 2017, 7, , 579; doi:10.3390/app7060579

	Source filament (averaged over 3 samples) (ppm)	Printed PLA (averaged over 3 areas) (ppm)
P	2100±50	1183±70
Ca	528±40	585±25
Si	310±35	180±15
Cr	110±10	61±5
Ti	80±10	40±10
Cu	35±10	13±4
Sn	(below detection)	18±5
Trace amounts of W, Cd, Zr, Nb, Mo		

Table 1: Results of XRF measurements from PLA natural source filament and printed PLA

While significant P appears in the sample, it is not likely to be the source of fluorescence unless it is present as phosphate. However, the Raman and FTIR spectra (shown below) do not indicate the presence of phosphate, nor is there a significant signal associate with silica. Calcium carbonate, a common additive in processing of polymers, may account for the Ca found (and is in agreement with evidence from Raman and FTIR spectroscopy). However, $CaCO_3$ alone does not fluoresce under irradiation at 405 nm. It does however fluoresce if reacted with organic ligands or if containing trace amounts of transition metal ions (19). Therefore it is possible that the fluorescent particles seen represent a form of calcium carbonate which has reacted with organic ligands (from PLA or other unknown additives) or due to association with trace amounts of transition metal contaminants. The concentration of fluorescent particles in voids may

indicate that whatever process resulted in the formation of voids also resulted in preferential retention or formation of $CaCO_3$ – based particles. It has also been found that inclusion of additives such as pigments in PLA may themselves cause the formation of small voids (20). As we will discuss, the presence of carbonate may have important implications for biomedical applications of printed PLA structures.

Raman Spectroscopy

Figure 5 shows the comparison of the full spectra of PLA spool material and printed PLA. The spectra look very similar and show minimal intensity changes. Peak assignments were made

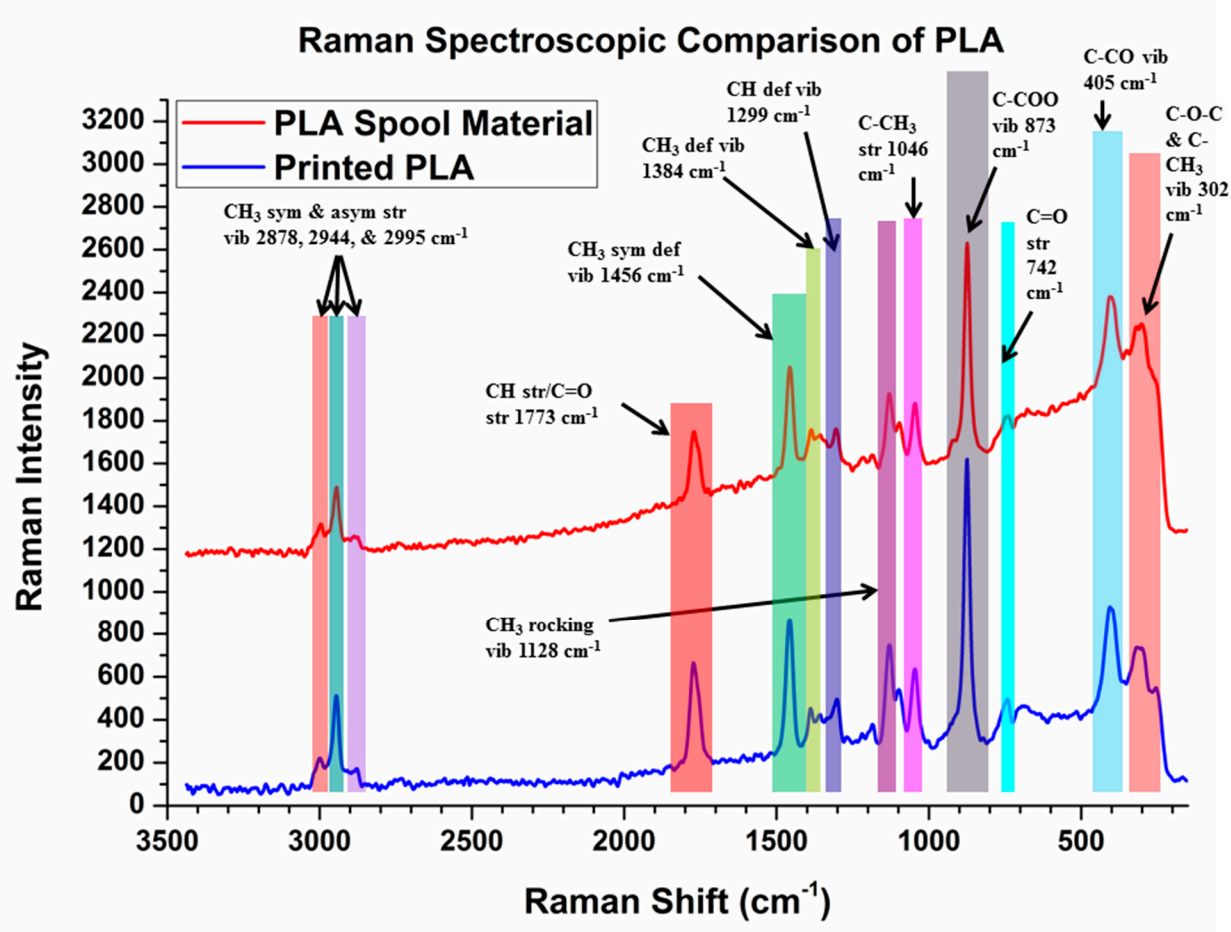

Figure 5: Raman spectroscopic comparison of PLA Spool material, printed PLA.

using Socrates; Suzuki; and Kister, (21-23), respectively. Peaks similar in all spectra include: CH_3 vibrations assigned to asymmetric stretching at 2995 -3002 cm^{-1} and, symmetric stretching 2944 -2947, and 2878 -2889 cm^{-1}. CH stretching/ C=O stretching at 1769-1773 cm^{-1}, CH_3 symmetric deformation vibration at 1454-1456 cm^{-1}, CH_3 rocking vibration assigned to 1128 cm^{-1}, C-O-C stretching assigned to 1095-1098 cm^{-1}, C-CH_3 stretching at 1042-1046 cm^{-1}, C-COO vibration assigned to 873 cm^{-1}, (possibly due to the presence of $CaCO_3$), C=O stretching assigned to 742 cm^{-1}, C-CO vibrational states assigned to 399-408 cm^{-1}, and C-O-C + C-CH_3 vibration assigned to 302-315 cm^{-1}.

Intensity changes following printing are seen in the highlighted regions of figure 3, including changes in the CH_3 deformation vibration at 1383-1387 cm^{-1}, and the CH deformation vibration peak at 1299-1305 cm^{1}. The light blue highlighted region of figure 3 shows an increase in the intensity of the C=O deformation peak at 742 cm^{-1} after printing the PLA. This suggests that the printing process of PLA increases the relative abundance of the C=O ligand, considered a primary active binding site in PLA. At the moment we suspect that calcium in the form of calcium carbonate may be responsible for the peaks assigned to 679 cm^{-1}, 873 cm^{-1}, and 1085 cm^{-1}, all of which are present in the spool material and printed PLA test samples. It will be shown below that spectral features associated with calcium-related groups are also present in the FTIR spectra of the spool material and the printed PLA.

Diffuse Reflection FTIR (DRIFTS):

Using diffuse reflectance FTIR (DRIFT) we compared the PLA spool material and the PLA material after printing. The FTIR spectrum collected from the PLA spool material, figure 6, is of somewhat lower intensity as compared to the other spectra, likely due to difficulties in analytical

Preprints (www.preprints.org) | NOT PEER-REVIEWED | Posted: 3 April 2017 doi:10.20944/preprints201704.0010.v1

Peer-reviewed version available at Appl. Sci. 2017, 7, , 579; doi:10.3390/app7060579

sampling configuration for the filaments. It also shows a number of differences as compared to

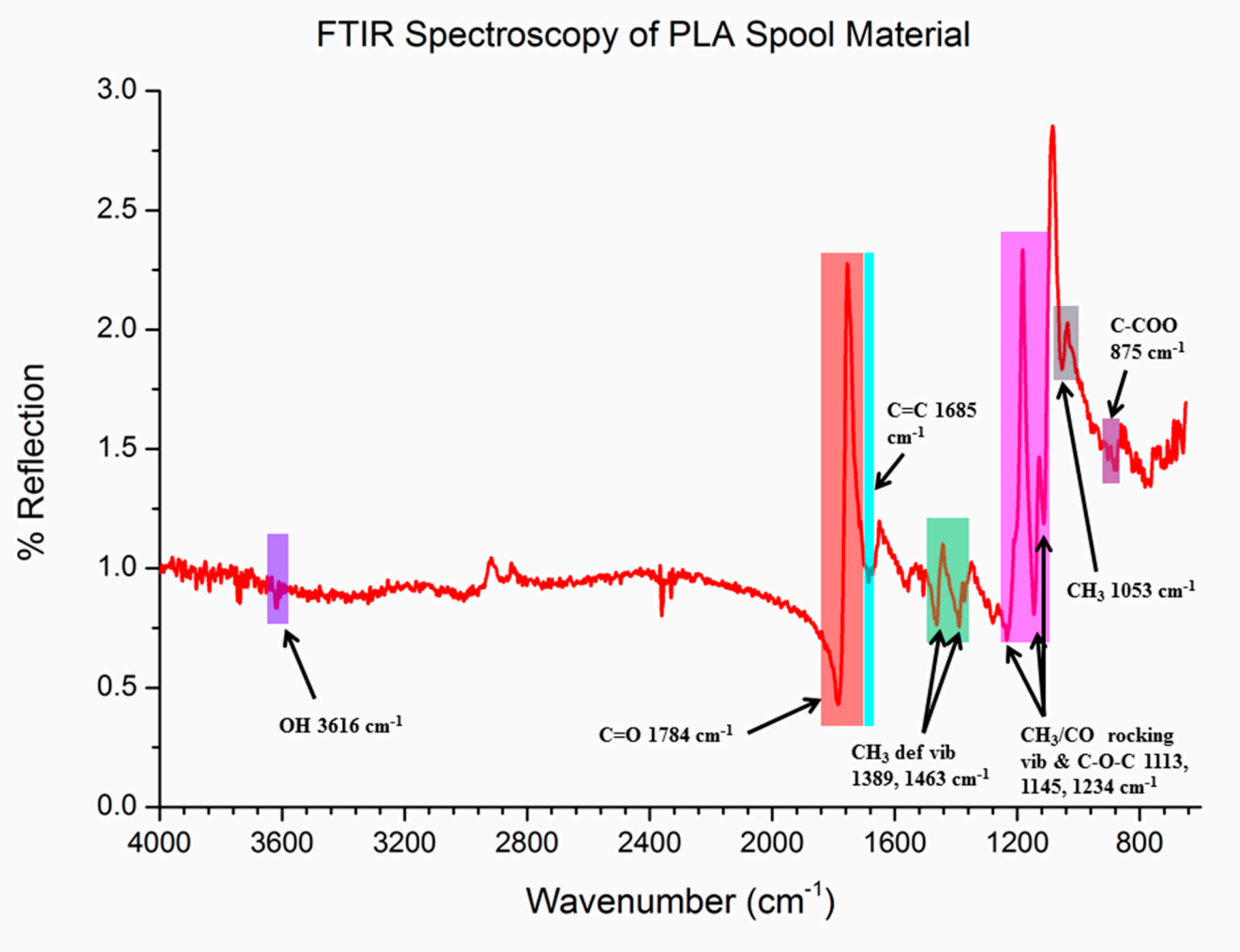

Figure 6: DRIFTS Spectroscopy of PLA spool material as received.

spectra from post-printed surfaces.

Peaks of interest from the PLA spool material include: a C-COO peak at 875 cm^{-1} (which can also be attributed to $CaCO_3$ as found in the Raman spectroscopic analysis); a CH_3 peak at 1053 cm^{-1} ; and CH_3/CO rocking vibrations with overlapping C-O-C stretching at 1113, 1145, and 1234 cm^{-1}. Other CH_3 deformation vibrations occur at 1389 and 1463 cm^{-1}. There is a peak associated with the C=C bond at 1685 cm^{-1} and a sharp, strong C=O peak at 1784 cm^{-1}. There is

also a small OH peak at 3616 cm^{-1} which overtime becomes more pronounced, as PLA spool material was discovered to be hygroscopic in nature.

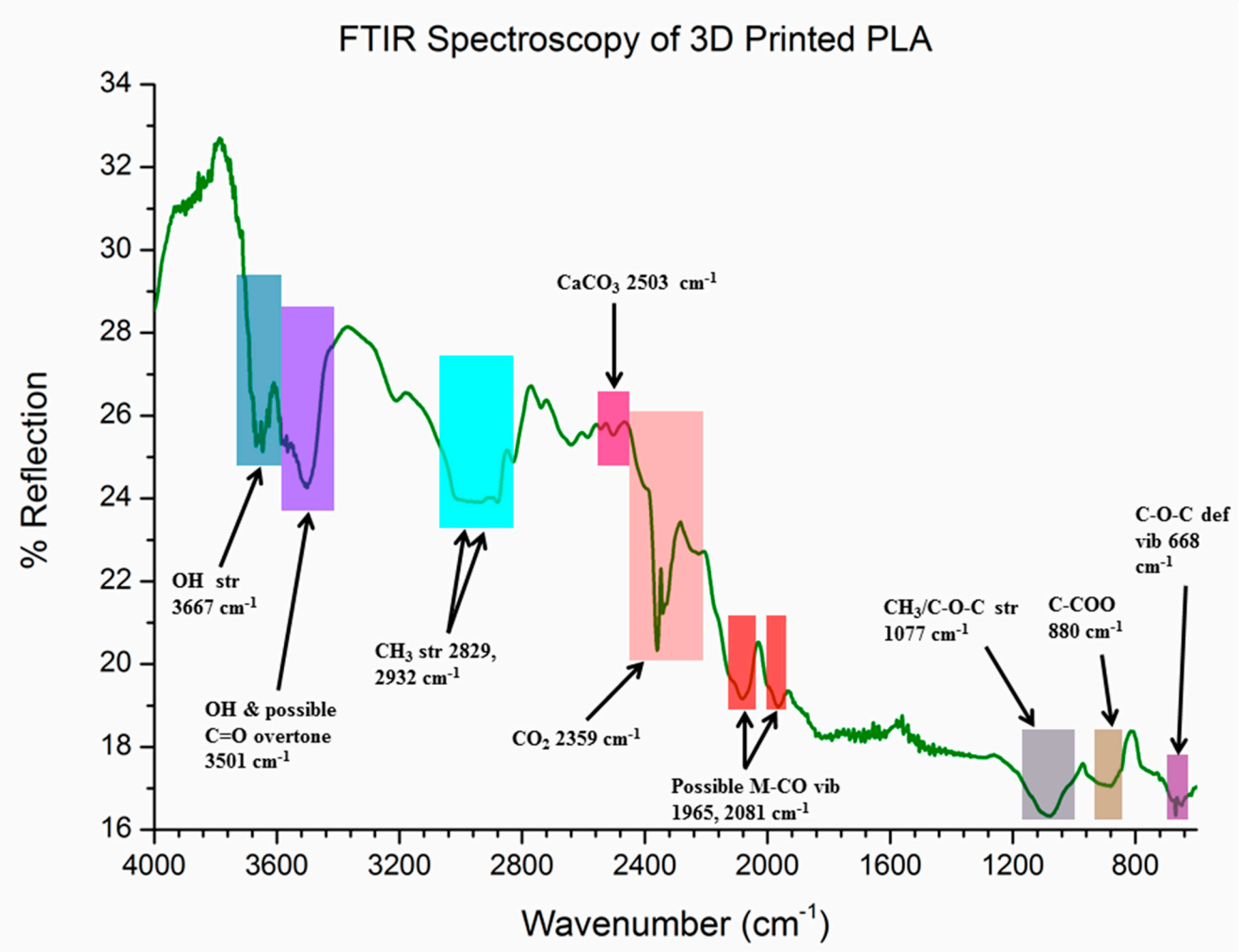

Figure 7: DRIFTS Spectroscopy of 3-D printed PLA.

A number of chemical changes were observed as the PLA spool material is heated to 230°C, is extruded, and then cools and recrystallizes, significantly changing bonding at least in the near surface region of the printed PLA. Some characteristic peaks in printed PLA test samples (figure 7) are: the C-O-C deformation vibration at 668 cm^{-1}; the CH_3 deformation with overlapping C-O-C stretching as 1077 cm^{-1}; and the C-COO peak at 880 cm^{-1} - which can be

associated with $CaCO_3$ (which is also indicated by the peak at 2503 cm^{-1}). This shows that the calcium carbonate-based additive indicated by the Raman spectra and FTIR of the spool material was retained after the printing process. Finding calcium carbonate in the PLA is significant due to the fact that PLA can also be used as support structure material for growing cells (24), and calcium is a required element for the growing cells. Other peaks in printed PLA include: the CH_3 stretching vibrations at 2829 and 2932 cm^{-1} and OH stretching vibrations at 3501 and 3667 cm^{-1} due to the hygroscopic nature of PLA (although these features can also be attributed to the C=O overtone stretching vibration at 3501 cm^{-1}). Also, there is an increase in CO_2 possibly due to a partial breakdown on calcium carbon to CaO and CO_2 which becomes bound the printed PLA material (see XPS of 3D printer PLA). There are two vibrations at 1965 and 2081 cm^{-1} that may be possible M-CO vibrations. These two M-CO vibrations may be due to metal contamination formed during the extrusion process.

Differential Scanning Calorimetry

Figure 8 shows a DSC graph of heat flux (mW) versus temperature(°C) for the PLA spool material and the printed PLA, Of the two samples, the PLA spool material has the highest glass transition temperature (T_g) at 57.7°C and the highest crystallinity temperature at 110.7 °C, but has the lowest melting temperature (T_m) at 155.1 °C, making the spool material ideal for 3 D printing via FDM (23, 24).

The act of extruding and printing the PLA at a system temperature of 230°C, significantly changes the glass transition (T_G) temperature, lowering it to 53.1°C, and also lowers the crystallinity temperature to 90.2 °C, but raises the melting temperature (T_m) to 166.7 °C.

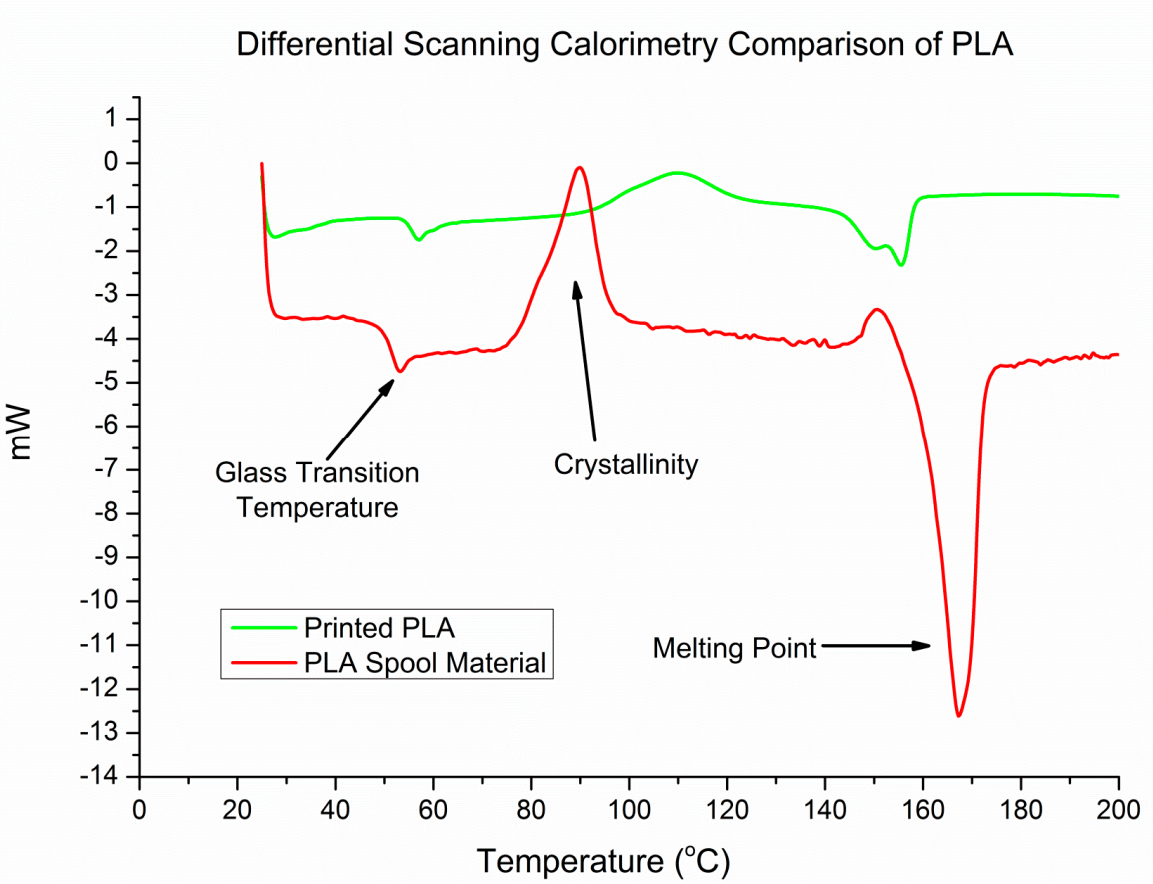

Figure 8: Differential scanning calorimetry (DSC) comparison of PLA spool material and printed PLA.

The lower crystallinity temperatures are the result of amorphous material in the filament becoming more ordered, resulting in crystallization structures forming during the cold crystallization part of testing. The melting temperature increases following printing, indicating greater ordering in the material.

X-ray Photoelectron Spectroscopy (XPS)

The presence of a Ca2p photoelectron peak in the XPS spectra of as received PLA spool material, figure 9, indicates the presence of calcium (at least in the surface region). The high resolution scan of the Ca2p photoelectron region is consistent with $CaCO_3$ (Ca $2p_{3/2}$/Ca $2p_{1/2}$ binding energy of 346.9 eV/350.8 eV). The C 1s peak deconvolution shows the presence of C-C/C-H at 285.3 eV, C-OH at 286.3 eV, and O-C=O at 289.3 eV. These peaks are consistent with

Preprints (www.preprints.org) | NOT PEER-REVIEWED | Posted: 3 April 2017 doi:10.20944/preprints201704.0010.v1

Peer-reviewed version available at Appl. Sci. 2017, 7, , 579; doi:10.3390/app7060579

PLA as well as carbonate, though the high intensity of the peak at 285.3 eV most likely represents additional hydrocarbons present on the surface of the spool material. These

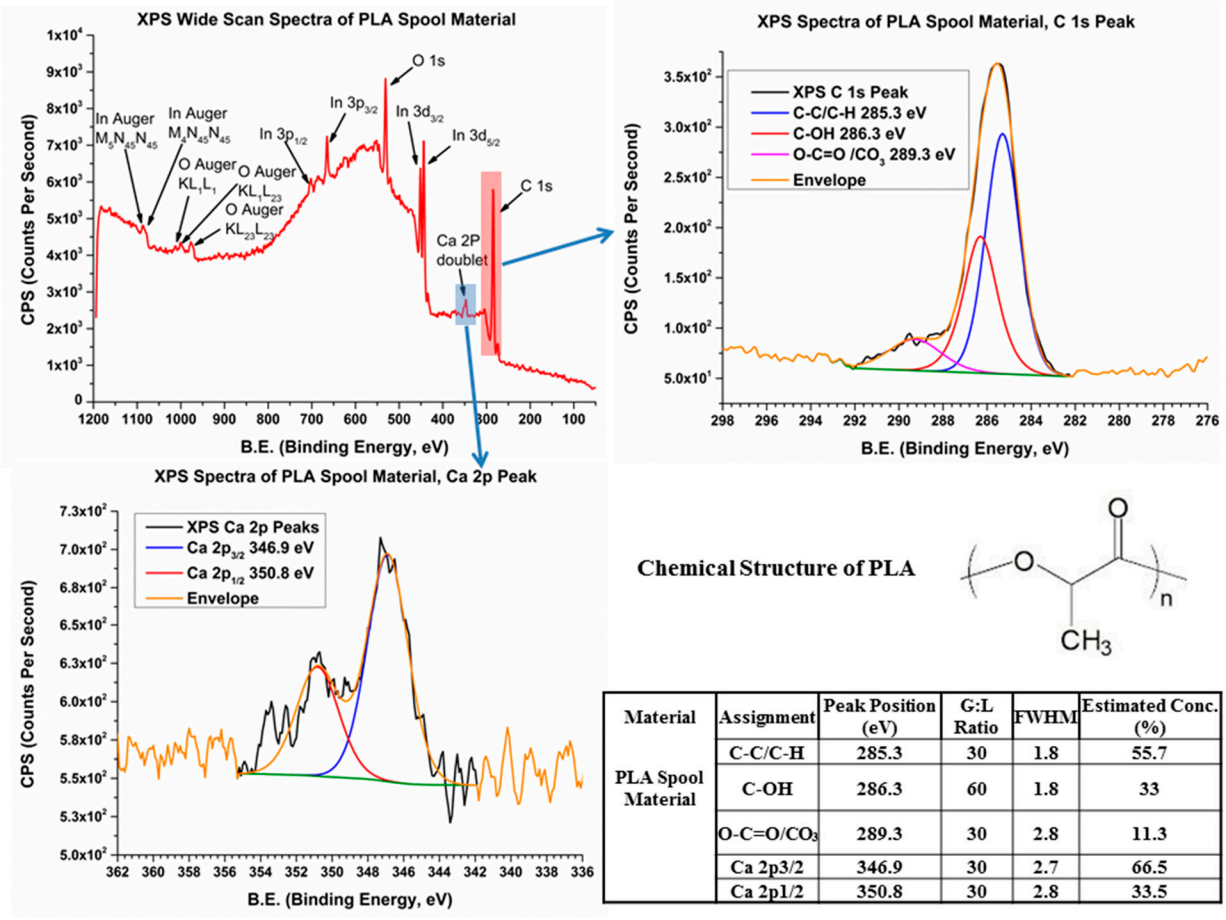

Material	Assignment	Peak Position (eV)	G:L Ratio	FWHM	Estimated Conc. (%)
PLA Spool Material	C-C/C-H	285.3	30	1.8	55.7
	C-OH	286.3	60	1.8	33
	O-C=O/CO3	289.3	30	2.8	11.3
	Ca 2p3/2	346.9	30	2.7	66.5
	Ca 2p1/2	350.8	30	2.8	33.5

Figure 9: XPS spectra of PLA spool material as received, showing the wide scan spectra and analysis of the C 1s and Ca 2p photoelectron peaks.

hydrocarbons can be associated with a coating layer used in storage, winding or handling during the manufacturing process. It is believed that calcium carbonate in the PLA spool material is also due to the manufacturing process as a component to aid in the extrusion and overall stability of the PLA filament.

XPS analysis of printed PLA, figure 10, indicates that calcium carbonate remains present on the surface of the despite extrusion conditions (melting at 230C and cooling rapidly to room temperature following printing). The C 1s spectrum deconvolution shows a ratio of C-C/C-H

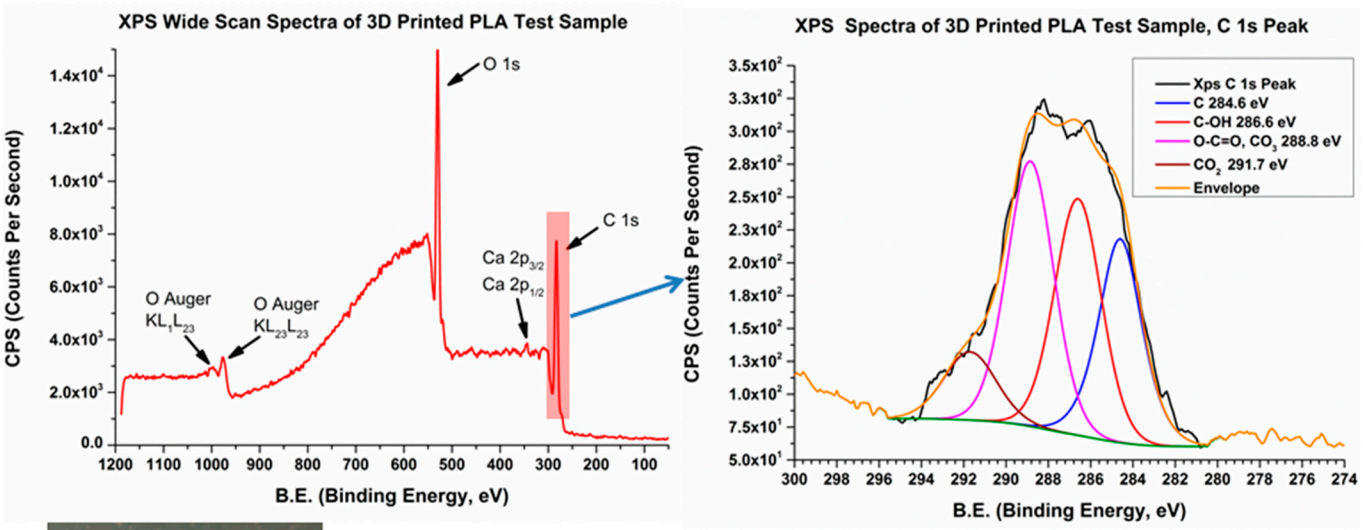

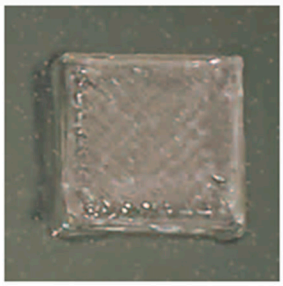

3D printed PLA test samples (10mm x 10mm x 2mm) made on a Makerbot Replicator 2 at standard resolution. Calcium carbonate is still present after printing.

Material	Assignment	Peak Position (eV)	G:L Ratio	FWHM	Estimated Conc. (%)
3D Printed PLA	C	284.6	60	2.4	25.3
	C-OH	286.6	30	2.6	30.6
	O-C=O/CO_3	288.8	30	2.6	34.3
	CO_2	291.7	30	2.9	9.8

Figure 10: XPS spectra of 3-D printed PLA test samples, showing the wide scan spectra, and the analyzed C 1s photoelectron peak, along with an image of the test sample analyzed by XPS.

(284.6 eV), C-OH (286.6 eV), and O-C=O (288.8 eV) closer to what one would expect from PLA with some additional enrichment of the higher energy peak due to the remaining presence of CO_3. However, the C 1s spectrum from printed PLA now also shows a peak at 291.7 eV. We

attributed this new peak to CO_2^-, which was seen to have a slightly elevated presence in the FTIR spectrum from printed PLA. While some CO_2 is noted by FTIR due to normal atmospheric conditions (as in the case of most materials) the presence under UHV (Ultra High Vacuum) conditions (10^{-9} - 10^{-10} torr) during XPS indicates some additional incorporation and sorption in the surface layer of the printed PLA. This is likely due to the decomposition of $CaCO_3$:

$$CaCO_3 \leftrightarrow CaO + CO_2 \qquad \text{Eq. (2)}$$

Therefore the increase in CO_2 seen in both the FTIR and this XPS spectra indicates that calcium carbonate is breaking down slightly and, due to the porous nature of printed PLA, it is likely becoming trapped (and subsequently chemisorbed) in the pores and voids of the material. This is consistent with results observed from laser confocal microscopy of the printed materials.

Conclusions

In this study we have explored the chemical, thermal and morphological changes that occur to PLA from source material to finished product. We discovered that the spool (source) material used contains a calcium carbonate-based additive which is retained following printing and in fact becomes concentrated in pores or voids. Since the carbonate-based particulates are found to fluoresce, it is likely that they are in some way reacted with polymer components or with trace transition metals found to be present in the filament. While there will obviously be differences between source material from different manufacturers, and hence potentially different additives, pigments and fillers, this study indicates the importance of complimentary characterization tools to understand the chemical transformations associated with possible additives and contaminants. In addition, our results indicate chemical changes in PLA (indicated by changes in the vibrational frequencies associated with CH_3, C-O-C, and C=O ligands) following 3d printing.

Our results also showed increases in the amount of OH ligands present most likely due to absorbed water not only from our application methods, but also from atmospheric adsorption as these experiments were conducted under normal conditions of temperature, pressure and humidity. Our current studies require scrutinizing these changes in chemistry as it is likely to affect the use of these structures as scaffolding for cell growth.

Heating, melting, and recrystallization of the PLA as a function of the printing process drastically changed the nature of the PLA, making it stronger (via tensile testing measurements) and more chemically reactive (indicated by the increase in abundance of the C=O ligand). However, while this more chemically reactive nature is of value for *in situ* synthesis and stabilization of metal nanoparticles (25) or for use as support structure for growth and calcification of cells, it also results in some disadvantages, such as increased susceptibility to water, alcohol, acetone and heat. Water will decompose the material over time and alcohols, acetone and heating will degrade the printed material as well (26-30). This means that sterilization with alcohol may alter the chemistry of 3d printed PLA samples. Also, PLA cannot be sterilized in an autoclave as both chemical alteration and degradation of the PLA will result. However, future testing of the PLA materials will look into using an FDA (Food and Drug Administration) approved gas (ethylene oxide) used for sterilization of medial materials that cannot be subjected to alcohols or heat. Preliminary testing has also been conducted on PLA test samples with *in situ* synthesized metal nanoparticles with minor to no observable degradation of the printed PLA structures themselves – such a method will enhance the usefulness of these 3d printed products for the medical industry (31).

Acknowledgement

The undergraduate students who participated in this work were supported by an NSF-EEC REU site grant, "REU Site for Nanotechnology in Health, Energy and the Environment", award 1359167 (Dr. Mary Poats, program officer). The authors would also like to acknowledge and thank Dr. James Quinn for assistance with the scanning electron microscopy, and Dr. Clive Clayton for guidance, helpful advice, and additional support.

References

(1) Lipson, Hod; Kurman, Melba; *Fabricated: The New World of 3D Printing*, Wiley, 2013.

(2) Garlotta, Donald; A Literature Review of Poly(Lactic Acid), *Journal of Polymers and the Environment*, **2002**, 9, No. 2.

(3) Henton, David E.; Gruber, Patrick; Lunt, Jim; Randall, Jed; *Polylactic Acid Technology, Natural Fibers*, Biopolymers, and Biocomposites, 2005, Chapter 16, 527-578.

(4) Athanasiou, Kyriacos A.; Niederauer, Gabriele G.; Agrawal, C. Mauli; Sterilization, Toxicity, Biocompatibility and Clinical Applications of Polylactic Acid/Polyglycolic Acid Copolymers, *Biomaterials*, **1996**, 17, 93-102.

(5) Proikakis, C.S.; Tarantili, P.A.; Andreopoulos, A.G.; The role of Polymer/Drug interactions on the Sustained Release from Poly(D, L-Lactic acid) Tablets, *European Polymer Journal,* **2006**, 4, No. 12, 3269-3276.

(6) Kulkarni, R.K.; Pani, K.C.; Neuman, C.; Leonard, F.; Polylactic Acid for Surgical Implants, Technical Report 6608, U.S. Army Medical Biomechanical Research Laboratory, Walter Reed Army Medical Center, Washington D.C., April 1966.

(7) de Faria, D. L. A.; Silva, Venancio S.; Oliveira, M. T., Raman Microspectroscopy of Some Iron Oxides and Oxyhydroxides, *Journal of Raman Spectroscopy,* **1997**, 28, 873-878.

(8) Hanesch, Monika; Raman Spectroscopy of Iron Oxides and (oxy)hydroxides at Low laser Power and Possible Applications in Environmental Magnetic Studies, *Geophysics International,* **2009**, 177, 941-948.

(9) Liang Luo; Christopher Wilhelm; Christopher N. Young; Clare P. Grey; Gary P. Halada; Kai Xiao; Ilia N. Ivanov; Jane Y. Howe; David B. Geohegan; Nancy S. Goroff, Characterization and Carbonization of Highly Oriented Poly(diiododiacetylene) Nanofibers, *Macromolecules*, **2011**, 44, 2626-2631.

(10) Savutsky; Golay, M. J. E., Smoothing and Differentiation of Data by Simplified Least Squares Procedures, *Analytical Chemistry,* **1964**, 36, No. 8.

(11) Sherwood, P. M. A., *In Practical Surface Analysis*, Briggs, D.; Seah, M. P., Eds.; Wiley, John and Sons: New York, 1993.

(12) Halada, G. P.; Clayton, C. R.; Comparison of Mo-N and W-N Synergism During Passivation of Stainless Steel through X-ray Photoelectron Spectroscopy and Electrochemical Analysis, *Journal of Vacuum Science and Technology, A,* **1993**, 11, 2342.

(13) Halada, G. P.; Kim, D.; Clayton, C. R.; The Influence of Nitrogen on the Electrochemical Passivation of High Ni Stainless Steels and Thin Mo-Ni Films, *Corrosion,* **1996**, 52, 36.

(14) Chidambaram, D; C.R. Clayton; G.P. Halada, A Duplex Mechanism-Based Model for the Interaction Between Chromate Ions and the Hydrated Oxide Film on Aluminum Alloys, *Journal of The Electrochemical Society* **2003**, 150 (5), B224-B237

(15) Solarski, S.; Ferreira, M.; Devaux, E.; Charicterization of the Thermal Properties of PLA Fibers by Modulated Differential Scanning Calorimetry, *Polymer,* **2005**, 46, No. 25.

(16) Giannitelli, S.M.; P. Mozetic; M. Trombetta; A. Rainer, Combined additive manufacturing approaches in tissue engineering, *Acta Biomaterialia*, **2015**, 24(15), 1-11

(17) Wang, Mian; Pelagie Favi; Xiaoqian Cheng; Negar H. Golshan; Katherine S. Ziemer; Michael Keidar; Thomas J. Webster, Cold atmospheric plasma (CAP) surface nanomodified 3D printed polylactic acid (PLA) scaffolds for bone regeneration, Acta Biomaterialia, **2016**, 46, 256-265

(18) Vasquez, M Jaime; J.R. Kearns; G.P. Halada; C.R. Clayton, Spatially resolved microchemical analysis of chromate-conversion-coated aluminum alloy AA2024-T3, *Surface and Interface Analysis* **2002**, 33 (10-11), 796-806.

(19) Berg, B.L.; J. Ronholm; D. M. Applin; P. Mann; M. Izawa1; E. A. Cloutis; L. G. Whyte, Spectral features of biogenic calcium carbonates and implications for astrobiology, *International Journal of Astrobiology* **2014**, 13 (4), 353–365.

(20) Roberson, David A.; Carmen R. Rocha; Monica Piñon, Evaluation of 3D Printable Sustainable Composites, Available online at https://sffsymposium.engr.utexas.edu/sites/default/files/2015/2015-75-Roberson.pdf (accessed 3-15-2017)

(21) Socrates, George; *Infrared and Raman Characteristic Group Frequencies, Tables and Charts*, 3rd edition, John Wiley and Sons, 2001.

(22) Suzuki, T.; Takahashi, K.; Uehara, H., Yamanobe, T.; Applications and Analysis of a DSC-Raman Spectroscopy for Indium and Poly(lactic acid), *J. Therm Anal Calorim,* **2013**, 1543-1549.

(23) Kister, G.; Cassanas, G.; Vert, M.; Effects of Morphology, Conformation and Configuration on the IR and Raman Spectra of Various Poly(lactic acid)s, *Polymers,* **1998**, 39, 267-273.

(24) Hutmacher, Dietmar W.; Scaffolding in Tissue Engineering Bone and Cartilage, *Biomaterial,* **2000**, Vol. 21, 2529-2543.

(25) Halada, Gary P.; Jha, Prashant; Cuiffo, Michael A.; Acquah, Kweku; Carl, Sarah; Aqueous Electrochemical Synthesis of Stable Silver Metal Nanoparticles onto a Chitosan Matrix on Stainless Steel, *ECS Transactions,* **2014**, 58, No. 42, 19-32.

(26) Li, Suming; McCarthy, Stephen; Further investigations on Hydrolytic Degradation of Poly (DL-Lactide), *Biomaterial,* **1999**, 20, 34-44.

(27) de Jong, S. j.; Arias, E,R.; Rijkers, D. T. S.; van Nostrum, C.F.; Kettenes-van den Bosch, J. J.; Hennink, W. E.; New Insights into Hydrolytic Degradation of Poly (lactic acid) Participation of the Alcohol Terminus, *Polymers,* **2001**, 42, 2795-2802.

(28) Al-Itry, Racha; Lamnawar, Khalid; Maazouz, Abderrahim; Improvement of Thermal Stability, Rheology and Mechanical Properties of PLA, PBAT and Their Blends by Reactive Extrusion with Functionalized Epoxy, *Polymer Degradation and Stability,* **2012**, 97, 1898-1914.

(29) Carrasco, F.; Pages, P.; Gámez-Pérez, J.; Santana, O. O.; Maspoch, M. L.; Processing of Poly(lactic acid): Characterization of chemical Structure, Thermal Stability and Mechanical Properties, *Polymer Degradation and Stability,* **2010**, 90, 116-125.

(30) Yuzay, Isinay, E.; Auras, Rafael; Soto-Valdez, Herlinda, Selke; Susan; Effects of Synthetic and Natural Zeolites on Morphology and Thermal Degradation of Poly(lactic acid) Composites, *Polymer Degradation and Stability,* **2010**, 95, 1769-1777.

(31) Ventola, C. Lee; Medical Applications for 3D Printing: Current and Projected Uses, *Pharmacy & Therapeutics,* **2014**, 39, No. 10, 700-711.